High-Performance and Industrially Viable Nanostructured SiOx Layers for Interface Passivation in Thin Film Solar Cells

Peer-reviewed author version

Cunha, Jose M. V.; Oliveira, Kevin; Lontchi, Jackson; LOPES, Tomas; Curado, Marco A.; Barbosa, Joao R. S.; Vinhais, Carlos; Chen, Wei-Chao; Borme, Jerome; Fonseca, Helder; Gaspar, Joao; Flandre, Denis; Edoff, Marika; Silva, Ana G.; Teixeira, Jennifer P.; Fernandes, Paulo A. & Salome, Pedro M. P. (2021)
High-Performance and Industrially Viable Nanostructured SiOx Layers for Interface Passivation in Thin Film Solar Cells. In: Solar RRL, 5 (3) (Art N° 2000534).

DOI: 10.1002/solr.202000534
Handle: http://hdl.handle.net/1942/33598

High-performance and Industrially Viable Nanostructured SiO_x Layers for Interface Passivation in Thin Film Solar Cells

José M. V. Cunha, Kevin Oliveira, Jackson Lontchi, Tomás S. Lopes, Marco A. Curado, João R. S. Barbosa, Carlos Vinhais, Wei-Chao Chen, Jérôme Borme, Helder Fonseca, João Gaspar, Denis Flandre, Marika Edoff, Ana G. Silva, Jennifer P. Teixeira, Paulo A. Fernandes, and Pedro M. P. Salomé*

José M. V. Cunha, Kevin Oliveira, Tomás S. Lopes, Marco A. Curado, João R. S. Barbosa, Dr. Carlos Vinhais, Dr. Jérôme Borme, Helder Fonseca, Dr. João Gaspar, Dr. Jennifer P. Teixeira, Dr. Paulo A. Fernandes, Dr. Pedro M. P. Salomé
INL – International Iberian Nanotechnology Laboratory, Avenida Mestre José Veiga, 4715-330, Braga, Portugal
E-mail: jose.cunha@inl.int

José M. V. Cunha, Dr. Pedro M. P. Salomé
Departamento de Física, Universidade de Aveiro, Campus Universitário de Santiago, 3810-193, Aveiro, Portugal

José M. V. Cunha, Dr. Paulo A. Fernandes
i3N, Universidade de Aveiro, Campus Universitário de Santiago, 3810-193, Aveiro, Portugal

Dr. Jackson Lontchi, Dr. Denis Flandre
Université Catholique de Louvain, ICTEAM institute, Place du Levant 3, 1348 Louvain-la-Neuve, Belgium

Tomás S. Lopes
Institute for Material Research (IMO), Hasselt University (partner in Solliance), Agoralaangebouw H, Diepenbeek, 3590, Belgium

Tomás S. Lopes
Imec division IMOMEC (partner in Solliance), Wetenschapspark 1, 3590 Diepenbeek, Belgium

Tomás S. Lopes
EnergyVille, Thorpark, Poort Genk 8310 & 8320, 3600, Belgium

Marco A. Curado
CFisUC, Department of Physics, University of Coimbra, P-3004-516, Coimbra, Portugal

Dr. Carlos Vinhais
Departamento de Física, Instituto Superior de Engenharia do Porto, Instituto Politécnico do Porto, Porto 4200-072, Portugal

Dr. Wei-Chao Chen, Dr. Marika Edoff
Ångström Laboratory, Solid State Electronics, Ångström Solar Center, Uppsala University, Uppsala SE-751 21, Sweden

Dr. Ana G. Silva
CEFITEC, Departamento de Física, Faculdade de Ciências e Tecnologia, Universidade Nova de Lisboa, Campus de Caparica, 2829-516, Portugal

Dr. Paulo A. Fernandes, Dr. Pedro M. P. Salomé
CIETI, Departamento de Física, Instituto Superior de Engenharia do Porto, Instituto Politécnico do Porto, Porto 4200-072, Portugal

Keywords: silicon oxide (SiO_x), passivation, ultrathin, $Cu(In,Ga)Se_2$ (CIGS), photolithography

In this work, it is demonstrated, by using industrial techniques that a passivation layer with nanocontacts based on silicon oxide (SiO_x) leads to significant improvements in the optoelectronical performance of ultrathin $Cu(In,Ga)Se_2$ (CIGS) solar cells. Two approaches were applied for contact patterning of the passivation layer: point contacts and line contacts. For two CIGS growth conditions, 550 ºC and 500 ºC, the SiO_x passivation layer demonstrates positive passivation properties, which were supported by electrical simulations. Such positive effects led to an increase of the light to power conversion efficiency value of 2.6 % (absolute value) for passivated devices compared to a non-passivated reference device. Strikingly, both passivation architectures present similar efficiency values. However, there is a trade-off between passivation effect and charge extraction, as demonstrated by the trade-off between V_{oc} and J_{sc} compared to FF. For the first time, a fully-industrial up-scalable process combining SiO_x as rear passivation layer deposited by chemical vapor deposition, with photolithography for line contacts, yields promising results towards high-performance and low-cost ultrathin CIGS solar cells with champion devices reaching efficiency values of 12 %, demonstrating the potential of SiO_x as a passivation material for energy conversion devices.

1. Introduction

Over the past decades, silicon wafer-based technology has been dominating the photovoltaic (PV) market, with thin film technology being a competitor with a relatively small market share.[1] Thin film technology is invariably looking to build up its competitiveness in the PV market, which will require innovative strategies to simultaneously increase performance and

decrease production costs. $Cu(In,Ga)Se_2$ (CIGS) based solar cells with a typical 2 μm absorber layer thickness stand out from its commercially available thin film counterparts, CdTe and amorphous silicon, presenting the highest light to power conversion efficiency value of all three technologies (23.35 %).[2,3] In order to pursue a prominent position in the market, a possible path is to further decrease the CIGS thickness to the ultrathin range (significantly lower than 1000 nm), where the most efficient devices in that range has a light to power conversion efficiency value of 11.8 % for a 240 nm thick,[4] 15.2 % for a 490 nm thick[5] and 17.5 % for a 900 nm thick[6] CIGS devices. The CIGS thickness reduction from the standard 2 μm to the ultrathin range will allow for a reduction in production costs by increasing machine throughput.[7,8] Moreover, the thickness reduction is in line with the recommendations from a recently conducted CIGS PV installations life cycle assessment study that encourages a continuous reduction on the rare metals usage.[9] Thus, allowing for lower production costs and also lower environmental impact. From a device performance point of view, keeping the conventional architecture with an ultrathin CIGS layer raises new optoelectronic concerns. Deterioration of the short-circuit current density (J_{sc}) values is consistently observed in ultrathin devices when compared to standard-thick ones.[10,11] In ultrathin devices, the thickness required for a complete optical absorption is effectively higher than the CIGS absorber layer thickness, leading to significant absorption losses in the near-infrared region (NIR). To overcome such optical losses, different light management schemes have been implemented.[12–16] However, the complexity of the CIGS optoelectronic properties and architecture of the device turns the integration of efficient novel designs into the CIGS solar cells challenging. A reduction of the CIGS layer thickness from the standard-thick to the ultrathin range will lead to a decreased charge carrier's mean path and an increased minority carrier generation rate per unit volume.[17] Accordingly, an increased charge carrier concentration is observed, which will potentially allow for an open-circuit voltage (V_{oc}) increase.[17] Nonetheless, it will also increase the minority charge carrier's likelihood of reaching the rear contact, increasing the probability of

recombination at this interface.[18] One approach to mitigate the recombination in the rear CIGS surface is focused on the use of an insulator passivation layer, in between the rear contact and the CIGS layer.[18,19,28,20–27] In order to establish electrical contact between CIGS and the rear electrode, nanocontacts are opened in the insulator layer, with e-beam lithography being commonly employed.[4,18,19,29] However, photolithography has the advantage of being cheaper and to have higher machine throughput compared to e-beam lithography. The referred advantages are highly desired for industrial processes, and, therefore, the photolithographic process up-scalability to the industry has the potential to be straightforward.

Several insulator materials, e.g. Al_2O_3, Si_3N_x, SiO_x, TiO_2, just to name a few, have been studied as passivation layers in the CIGS technology.[20,25,30–33] The prospect of using the same approach and insulator to passivate both front and rear interfaces of the same solar cell is very attractive from a fabrication perspective, and SiO_x emerges as a strong material to perform such role.[20,30,34] SiO_x presents promising properties that allow for its implementation as front and rear passivation layers, namely the ability to change the polarity values of the fixed insulator charges (Q_f) by manipulating the deposition parameters, enabling an efficient field-effect passivation of both minority and majority CIGS charge carriers.[30] It is even possible to change the density of interface active defects and the Q_f density, which is proven to be an essential parameter to accomplish a high-performance passivation layer.[35] Furthermore, SiO_x rear passivation employed with photolithography to open the nanocontacts has already been implemented with promising preliminary results.[20] Nonetheless, more comprehensive studies are necessary, to understand and establish an effective procedure to implement SiO_x as a passivation layer in the CIGS solar cells architecture. Furthermore, SiO_x has the potential to be used as a passivation layer in other thin film technologies, such as CdTe, Cu_2ZnSnS_4 (CZTS) or perovskites, which could allow for an effective defects passivation.[36,37,46,47,38–45]

In this study, point contacts and line contacts are used to implement two different SiO_x rear passivation architectures for CIGS based solar cells, with the intention of attaining high-

performance substrates. The point contacts will be produced by a laboratory e-beam lithography technique and the line contacts will be produced by an industrially viable photolithography technique. The use of two different patterning techniques is of utmost importance in this work, since the main objective is to understand if photolithography has the potential to produce devices with the same performance as e-beam lithography. Furthermore, the two passivated substrates are compared between them and against a conventional non-passivated substrate. The reference non-passivated device will be named as Ref, and passivated devices will be named as PointContact or LineContact following the respective passivation architecture. We note that in order to better comprehend the passivation layer effect on the performance increase compared to the conventional non-passivated substrate, the CIGS layer was not optimized, i.e. it did not use Ga-profile, post-deposition treatment or anti-reflective coating, so that the gains observed for the passivated substrates are effectively and only due to the passivation effect itself. The three substrates are integrated in CIGS based solar cells fabricated at 550 ºC (standard temperature) and 500 ºC. Therefore, it is possible to better understand the ability of the SiO_x layer to survive different CIGS growth temperatures, and, at the same time, determine if it retains its passivation properties. The integration of both passivated substrates in the CIGS solar cells architecture deliver an increase in the figures of merit compared with the conventional solar cell substrate. Electrical simulations coupled with morphological, structural and electrical characterizations of the fabricated devices are presented, allowing for an in-depth study of the SiO_x rear passivation properties on CIGS solar cells.

2. Characterization

In this work, CIGS was grown at two different temperatures, 550 ºC and 500 ºC, which will bring relevant insights into: i) the SiO_x ability to survive the harsh CIGS growth conditions (see the SEM analyses in the supporting information); and ii) the SiO_x performance as a passivation layer for each of the studied temperatures. Such study is needed as it is known that some

materials, such as SiO_x, do not maintain its properties at elevated temperatures.[48] The current density vs. voltage (J-V) figures of merit suggest that devices grown at 550 ºC have a higher optoelectronic performance with higher V_{oc}, fill factor (FF) and light to power conversion efficiency values, compared to respective devices grown at 500 ºC, as shown in Figure 1 a). The Ref device grown at 550 ºC achieved an average efficiency value of 8.8 %, whereas the equivalent device grown at 500 ºC attained an average efficiency value of 6.2 %. Looking to the average V_{oc} values, it decreases from 585 mV to 523 mV, from Ref grown at 550 ºC and 500 ºC, respectively, with FF values also decreasing from 66.9 % to 50.2 %. The figures of merit values increase for the Ref grown at 550 ºC is possibly related with better morphological and structural properties, due to i) larger CIGS grains with less grain boundaries, resulting of the higher CIGS growth temperature, as observed by SEM in the supporting information and as it was already reported in the literature;[49–51] and other effects such as ii) Ga depth distribution;[52,53] or iii) alkali dynamics,[49,54–57] just to name a few examples. The passivated devices grown at 500 ºC demonstrated the same electrical trends as the ones grown at 550 ºC, with all the SiO_x patterned devices having superior V_{oc} and efficiency values compared to the respective reference device. The V_{oc} increase is a clear indication that the insulator layer SiO_x acts as an effective rear passivation layer for CIGS solar cells. An important observation is that the SiO_x passivation effect is independent of the CIGS growth temperature, as shown by the improved figures of merit values of the passivated devices compared to the respective reference counterparts, as presented in Figure 1 a). Since similar trends were obtained for both temperatures, and for clarity, only detailed results of devices grown at 550 ºC will be analyzed henceforth. Therefore, only J-V plots measured under dark and illumination (Figure 1 b)), external quantum efficiency (EQE) plots (Figure 1 c)), as well as, diode parameters (Figure 1 d)) for the devices grown at 550 ºC are shown and analyzed. The figures of merit of all studied devices (Figure 1 a)) are still shown for a better understanding of the effective SiO_x passivation effect at different temperatures.

The J-V plots of the Ref and LineContact devices show a cross-over between dark and illuminated curves,[58] as shown in Figure 1 b). Such behavior is possibly related with an illumination-dependent voltage drop on a thin defect layer located on the CIGS absorber front surface.[59,60] PointContact device does not show a clear cross-over, since a roll-over behavior appears.[58] In CIGS solar cells, a roll-over has been observed when a rear sodium (Na) diffusion barrier is present.[55,61,62]

The PointContact device achieves a V_{oc} average value of 653 mV, which corresponds to a 68 mV increase over the Ref, and an average 10.5 % in power conversion efficiency values. Moreover, the respective PointContact champion cell attains an efficiency value of 12.0 %. From the EQE curves, presented in Figure 1 c), the J_{sc} increase over Ref is mostly localized in the NIR. The LineContact device achieves an average V_{oc} value of 639 mV, which corresponds to a 54 mV increase over the Ref. LineContact does not have the roll-over seen in the PointContact, which is translated into the highest average FF value of 74.7 % among the studied devices. As a result, LineContact device has the highest average efficiency value of 11.4 %, which is 2.6 % (abs.) higher than Ref. It is observed that even though LineContact device has a higher average efficiency value compared to PointContact device, the latter has a higher champion cell efficiency value, which is explained by a higher inhomogeneity, as observed by its higher standard deviation value. Regarding the inhomogeneity observed for the PointContact device, from the process point of view, it is more complex to produce holes with 150 nm than lines with 1100 nm. Since we are producing structures with a small diameter (150 nm), even though they are fabricated by the very well-established e-beam lithography process, the variation within the substrate will be higher compared to the lines produced by the industrial photolithography process. Therefore, it is shown that the LineContact process provides better homogeneity of the features throughout the substrate compared to the PointContact process.

a)	CIGS growth temperature (°C)	V_{oc} (mV)	EQE corrected J_{sc} (mA/cm^2)	FF (%)	Eff. (%)
Ref	550	585 ± 7 (597)	22.50 ± 0.44 (22.72)	66.9 ± 1.3 (69.8)	8.8 ± 0.4 (9.5)
PointContact	550	653 ± 13 (673)	24.23 ± 0.67 (24.77)	66.6 ± 2.6 (71.9)	10.5 ± 0.7 (12.0)
LineContact	550	639 ± 7 (652)	23.80 ± 0.21 (23.55)	74.7 ± 0.8 (76.4)	11.4 ± 0.2 (11.7)
Ref	500	523 ± 14 (537)	23.67 ± 0.85 (25.25)	50.2 ± 8.8 (60.8)	6.2 ± 1.3 (8.2)
PointContact	500	614 ± 21 (657)	23.99 ± 0.56 (25.16)	55.6 ± 3.2 (63.4)	8.2 ± 0.9 (10.5)
LineContact	500	588 ± 9 (600)	23.97 ± 0.45 (25.04)	65.9 ± 1.9 (69.2)	9.3 ± 0.5 (10.4)

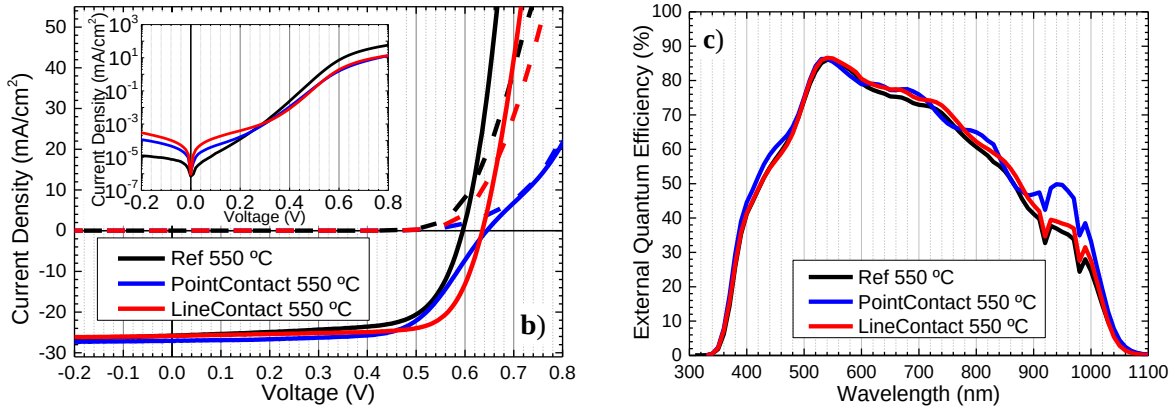

d)	R_p (Ω.cm^2)	R_s (Ω.cm^2)	A	J_0 (mA/cm^2)
Ref	326 ± 47	0.68 ± 0.06	1.25	(43.6 ± 10.1) x10^{-8}
PointContact	1573 ± 406	1.28 ± 0.18	1.45	(25.0 ± 12.3) x10^{-8}
LineContact	754 ± 95	0.66 ± 0.04	1.35	(6.97 ± 1.16) x10^{-8}

Figure 1 a) J-V figures of merit: averages and standard deviations values of all studied devices. Figures of merit values for the highest efficiency cells also presented in brackets. J_{sc} values calculated from the EQE spectra. Averages taken from 12 cells; b) Representative J-V plots of the device with the efficiency value closer to the efficiency average value. Straight lines are illuminated curves and dashed lines are dark curves. The inset figure is the dark log J-V curve; c) Representative EQE plots of the device with the J_{sc} value closer to the J_{sc} average value; and d) Solar cells' diode parameters average and standard deviation values for devices grown with a substrate temperature of 550 ºC. R_p stands for parallel resistance, R_s for series resistance, A for ideality factor and J_0 for saturation current density.

The devices' diode parameters are summarized in Figure 1 d). The possibility of shunt paths, common in ultrathin devices,[10,11,21,63] is reduced by the insulator used in the passivation layer, resulting in an increase of the parallel resistance (R_p) values of both PointContact and LineContact compared to the Ref device. PointContact presents a higher series resistance (R_s) compared to other devices possibly due to a reduced rear contact opening area, limiting carrier collection, which results in charge losses. Therefore, there is room for further optimization of

the rear passivation configuration in the point contact architecture. On the other hand, devices with line contact configuration have a higher contact area compared to PointContact devices, leading to a lower R_s average value. The shown roll-over for the PointContact device, which is affecting its FF values, is also affecting the ideality factor (A) value, as the PointContact device has the highest A value among the studied devices. The PointContact device shows higher V_{oc} values than LineContact, which is attributed to the higher SiO_x passivation area. The increased V_{oc} values over the reference device, indicates an effective interface defects passivation by the SiO_x layer for both passivation patterns, which is more pronounced for the device with the highest passivation area. The V_{oc} values increase is supported by the decrease of the saturation current density (J_0) value for both passivated devices compared to Ref (Figure 1 d)), strengthening the proof of the effectiveness of the rear interface passivation by the SiO_x passivation layer. Therefore, it is demonstrated the good SiO_x passivation, as the passivated device's V_{oc} and J_0 values indicate a lower recombination rate compared to the reference device.[64,65]

It is necessary to understand the Na effect on the devices' performance, and if the figures of merit values increase are only related with passivation effects and/or Na effects as well. Therefore, glow-discharge optical emission spectroscopy (GDOES) measurements were carried out to measure the in-depth Na profile for devices grown at 550 ºC, as shown in Figure 2 a). To better understand the Na concentration influence together with the SiO_x passivation effect on each device's optoelectronic properties, dark capacitance vs. voltage (C-V) measurements were conducted in order to get the net free carriers concentration (N_{cv}) and depletion region width (*W*) values for each device at the 0 V bias.[33,66,67] A representative N_{cv} against *W* plot, with varying bias, for each device, is shown in Figure 2 b) with the N_{cv} and *W* average and standard deviation values shown in the inset table of Figure 2 b). It is noted that the shown plot for each device is a representative curve, which might have different N_{cv} and *W* values compared to the respective average values presented in the inset table.

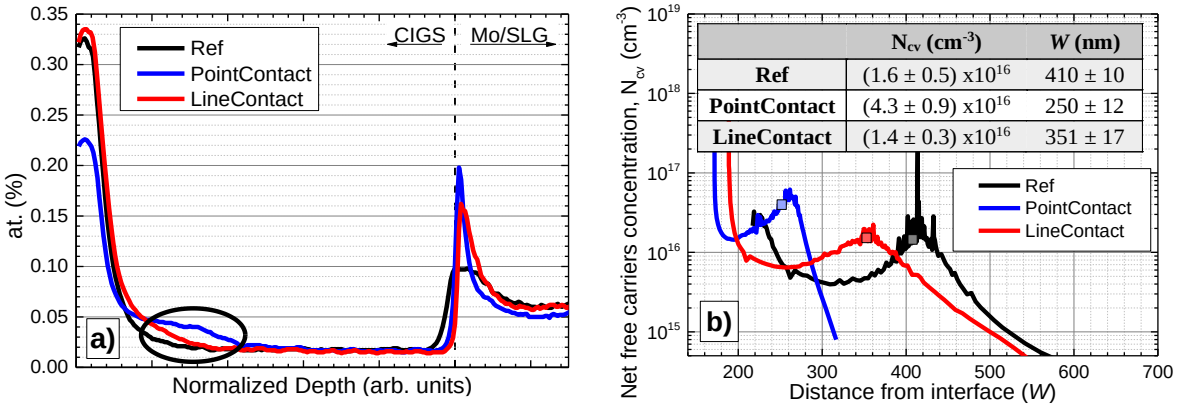

	N_{cv} (cm^{-3})	W (nm)
Ref	(1.6 ± 0.5) x10^{16}	410 ± 10
PointContact	(4.3 ± 0.9) x10^{16}	250 ± 12
LineContact	(1.4 ± 0.3) x10^{16}	351 ± 17

Figure 2 a) GDOES Na in-depth profile of devices grown with a substrate temperature of 550 ºC. The dashed vertical line is a guide to the eye representing where the CIGS/Mo interface is located; and b) Representative N_{cv} vs W plot of the device with the N_{cv} and W values closer to the N_{cv} and W average values. The depletion region and net free carrier concentration are taken at 0 V and are represented in square marks. Inset table represents the zero-bias average and standard deviation values of N_{cv} and W. Averages taken from 12 cells.

Analyzing the Mo/CIGS interface represented by the dashed line in Figure 2 a), it is clear that SiO_x forms a Na accumulation layer, where the PointContact architecture acts as a stronger Na accumulation layer than the LineContact, which is the repercussion of the significantly lower contact area of the PointContact compared with the LineContact architecture. Having in mind that for the passivation layers 15 nm NaF precursors layers were used as the Na source – a thickness value equal to the one of 2000 nm CIGS – it is hard to understand if such Na accumulation is evidence of a diffusion barrier behavior of in-diffusion (from the NaF into the Mo) or out-diffusion (from the glass to the CIGS). At a specific depth, it is observed a slightly Na concentration increase for the PointContact device, compared to the other studied devices, as represented by the circle in the graph. In order to understand which device has the highest Na concentration overall, secondary ion mass spectrometry (SIMS) measurements should be carried out.[68]

In Figure 2 b), it is shown that PointContact has the highest N_{cv} value of 4.3x10^{16} cm^{-3}, while the LineContact and Ref have approximately the same N_{cv} value. Ref device has the highest depletion region among the studied devices. The N_{cv} values are known to increase with Na concentration,[55,69] which is in accordance with the N_{cv} values extraction at 0 V bias being matched to the region in the Figure 2 a) represented by a circle for the PointContact device.

However, the N_{cv} values extraction at 0 V bias may have been extracted at a slightly higher depth values for both Ref and LineContact devices (considering the higher average *W* values for these two devices comparing to PointContact one, as shown in the inset table of Figure 2 b)) where both have approximately the same Na concentration (lower than PointContact). Therefore, the N_{cv} values increase for the PointContact should be related with the highest Na concentration observed for a specific region, compared to Ref and LineContact devices. The high passivation area in the PointContact device had a clear impact in the Na distribution in the CIGS layer.

3. Electrical simulations

Electrical simulations were performed in order to better understand the presented results and to study the SiO_x performance as a passivation layer. R. Kotipalli *et al.*[31] analyzed Metal-Insulator-Semiconductor (MIS) devices before and after annealing at ~500 ºC with selenium atmosphere to reproduce the CIGS growth. It was shown that the polarity of the Q_f values changed from positive (before exposure) to negative (after exposure).[31] Despite of the insulator in the study being alumina (Al_2O_3), the same phenomenon may be expected for the SiO_x case, since previous MIS studies without annealing also demonstrated positive charges in the SiO_x insulator.[30] Therefore, based on the previous studies, it was decided to simulate both SiO_x possible Q_f polarity signals, to better comprehend its impact on the devices' performance and to show the importance of the Q_f values control during the insulator deposition in order to maximize the final devices' performance. Q_f values of $+4x10^{11}$ cm^{-2} and $-8x10^{12}$ cm^{-2} were studied.[30,31] Such values were chosen to understand if the SiO_x layer has the ideal Q_f values, which should be around 10^{12}-10^{13} cm^{-2} or if the material has a Q_f value below the ideal one ~10^{11} cm^{-2}, as reported in the literature.[31,70,71] The contact width values were varied, and for a better understanding, the contact width values were converted into a percentage of passivation area using the following equations:[72]

$$Passivation\ area = \left[1 - \frac{(\pi d^2)}{4P^2}\right] \times 100 \quad (1)$$

$$Passivation\ area = \left[1 - \left(\frac{d \times P}{P \times P}\right)\right] \times 100 \quad (2)$$

where d is the contact width value and P is the pitch value. Equation (1) is for point contact architectures and equation (2) is for line contact architectures. The electrical simulations demonstrate V_{oc}, J_{sc}, FF and absolute efficiency gains of the passivated devices over the reference device, as shown in Figure 3. In this simulation, the presented gains are in comparison with a simulated non-passivated reference device, i.e. a gain equal to 0 represents the same performance as the reference device.[35]

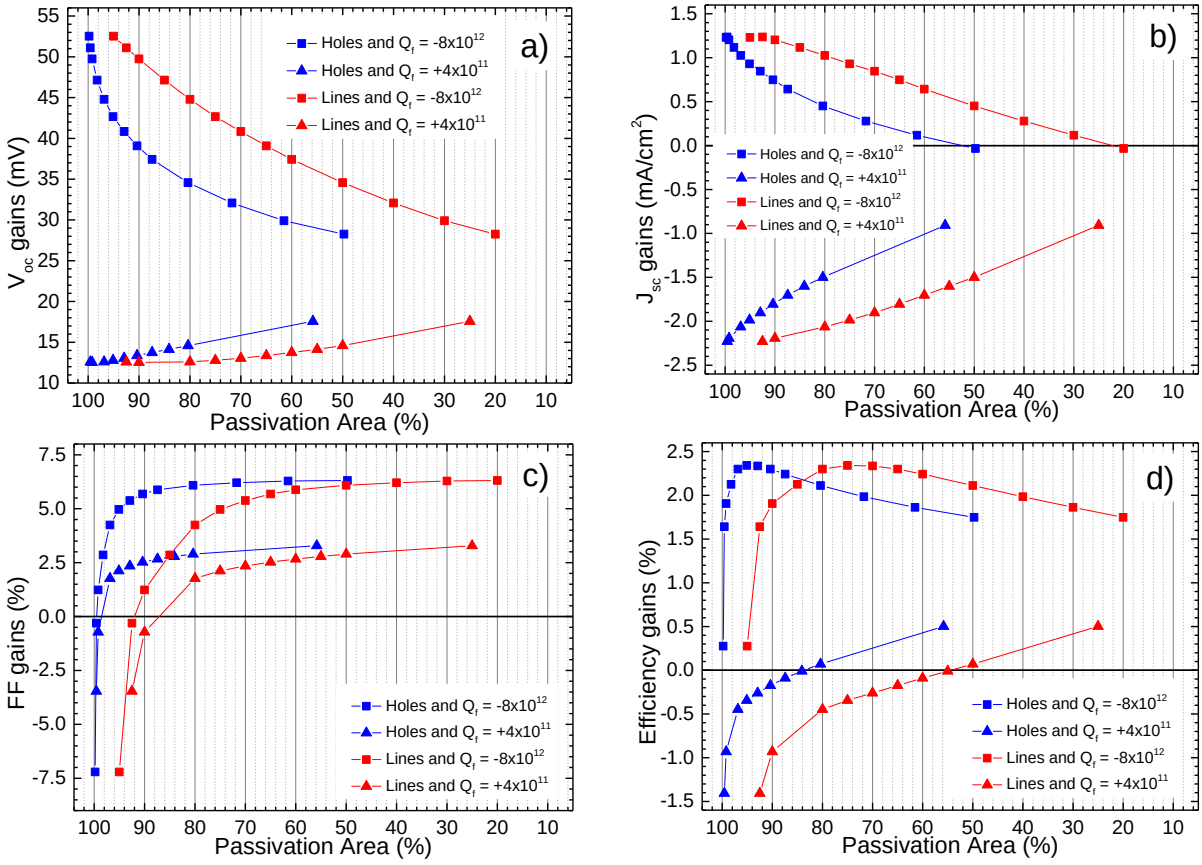

Figure 3 - Figures of merit absolute gains of the passivated devices over the reference device: a) V_{oc} gains; b) J_{sc} gains; c) FF gains; and d) Efficiency gains. Pitch value of 2000 nm simulated. Red lines correspond to the passivation area for line contacts and blue lines correspond to the passivation area for point contacts. Square marks represent a Q_f value of -8x10^{12} cm^{-2} and triangle marks represent a Q_f value of +4x10^{11} cm^{-2}.

The electrical simulations show that the solar cells performance optimization depends on the studied parameters, such as the Q_f value and respective polarity value, as well as the contact shape and passivation area. Negative Q_f values, represented by square marks in the graphs, show superior performance in all figures of merit compared to positive Q_f values, and therefore

only negative Q_f values will be analyzed henceforth. Considering negative Q_f values, the V_{oc} and J_{sc} values follow the same trend. Moreover, both figures of merit increased with higher passivation areas, as shown in Figure 3 a) and b). Such increase is expected, since, for higher passivation areas, the effective rear recombination rate is reduced. On the other hand, FF values, shown in Figure 3 c), have the opposite trend with values increasing for lower passivation areas. FF values are negatively affected by the contact opening width, since the FF values degrade when the contact opening is reduced and does not allow for efficient current extraction. Therefore, the FF values will increase when the contact area is increased, i.e. for reduced passivation area, and tend to saturate after the contact area is sufficiently large. Regarding efficiency gains (Figure 3 d)), this simulation shows that the optimum passivation area value for a passivation architecture with point contacts, represented by blue lines in the graph, is approximately 95 %. In contrast, the optimum value for a passivation architecture with line contacts, represented by a red line in the graph, is approximately 75 %. Such striking simulation results show the need to carefully design the passivation architecture, depending on the used contact shape, to account the optimal structure dimensions, in order to achieve the highest performance values. In our case, the PointContact device passivation area (99.7 %) has surpassed the optimal values, which translates into an efficiency drop and, according to the simulations, it is mainly due to FF losses. Therefore, the passivation area should be reduced to allow for effective charge collection. The LineContact device has less passivation area (59.5 %) than the found optimal values, which translates into a shortcoming in the efficiency value and, according to the simulations, it is mainly due to V_{oc} and J_{sc} losses. A remarkable outcome can already be considered: a line contact passivation area of 75 % is equivalent in terms of efficiency gains (~2.4 %) to a point contact passivation architecture with 95 % of passivation area.

4. Discussion

In this work, two different patterns were successfully produced on a SiO_x layer to be used as a rear passivation layer in ultrathin CIGS solar cells. Furthermore, two different CIGS deposition temperature values were tested to understand the resilience of the SiO_x passivation effect. Differences between the CIGS layers grown at 550 ºC and 500 ºC were found both at the grain and crystalline level, and are shown in detail by SEM and XRD analyses on the supporting information. Electrical measurements show that devices with point contacts, that have higher passivation area, presented increased V_{oc} values over devices with line contacts. On the other hand, the LineContact device that have higher contact area, have increased FF values over the PointContact device. The lower FF values for the PointContact device compared to the LineContact device observed in the J-V measurements, was supported by electrical simulations, which demonstrated that the PointContact device has room for further improvement by increasing the contact area, which will allow for increased FF values. The highest Na diffusion barrier effect observed in GDOES for PointContact device might suggest that PointContact device does not have an optimized Na concentration. Considering such hypothesis, the highest Na diffusion barrier effect observed in GDOES for PointContact devices supports the observed roll-over in the J-V analysis, as the roll-over might be related with the Na diffusion barrier. The observed roll-over also explains the low average FF value of PointContact device, as well as, its high standard deviation value. The PointContact ideality factor parameter value is also affected by the roll-over appearance, as it is the highest value among the studied devices. Despite of the observed Na barrier for the passivated devices, all devices had a Na pre-deposition treatment. However, the amount of deposited sodium fluoride (NaF) does not seem to be optimized for the used CIGS thickness and/or passivation architecture – as evidenced by the strong Na accumulation at the interfaces and the odd FF values indicating that a more efficient Na introduction strategy needs to be developed. GDOES measurements may have matrix effects that may cause artifacts to appear,[73] and, therefore, the absolute quantity of Na

and its distribution on the CIGS layer should not be considered by GDOES measurements alone. Consequently, in order to further understand the effect of the passivation layer on the Na distribution in the CIGS and the effects on final devices, more measurements, such as SIMS, X-ray photoelectron spectroscopy (XPS), Rutherford backscattering spectrometry (RBS) and Particle-induced X-ray emission (PIXE) should be carried out to complement the GDOES measurement.[74–78]

LineContact devices have higher collection area compared to PointContact devices, resulting in higher FF values in the J-V analysis, which ultimately results in the highest average efficiency values of the studied devices. Nonetheless, it was found that LineContact devices have lower V_{oc} values compared to PointContact devices due to a lower passivation area. Electrical simulations explain these results and show that LineContact devices have room for further improvement by increasing the passivation area, which will lead to higher V_{oc} values.

Comparing the illuminated and dark J-V measurements, it is observed that while the illuminated R_p value is lower for the Ref compared to PointContact and LineContact devices, the current density for Ref device observed in the dark J-V plot at -0.2 V is the lowest among the studied devices. The reason for the differences between the dark and light J-V plots is a complex topic, but it may be due to the light soaking treatment performed before the illuminated J-V measurements, which was not performed before the dark J-V measurements. Such differences may be related with light induced defects.[79–81] Moreover, even though the Ref device has the lowest R_p value together with the highest J_0 value, such parameters could not be physically correlated since they are extracted in different voltage regions and related to different operations. The PointContact device on its hand, has the highest R_p value, but it does not have the lowest J_0 value. In the C-V analysis, it was shown that the LineContact device has approximately the same N_{cv} value compared to Ref, and that the PointContact device has the highest N_{cv} average value of 4.3×10^{16} cm^{-3}. A possible hypothesis to explain the result is related with the region represented by a circle in Figure 2 a), where the PointContact device has the highest Na

concentration compared to the studied devices. Therefore, the highest N_{cv} value for the PointContact device is related with the Na concentration and distribution, as it is known that the N_{cv} values increase for devices with higher Na concentration.[55,69] However, it is not clear if the increase in the N_{cv} values fully explain the V_{oc} increase for the PointContact device. Therefore, it is necessary to calculate the expected V_{oc} gain that is provided by the N_{cv} increase for the passivated devices compared to Ref. Such V_{oc} gain provided by the N_{cv} values increase, will be hereafter named as ΔV_{oc}. In order to calculate ΔV_{oc}, the following equation was used:[18,82,83]

$$\Delta V_{oc} = \frac{k_B T}{q} \ln\left(\frac{N_{cv}(passivated)}{N_{cv}(reference)}\right) \quad (3)$$

where k_B is the Boltzmann constant, T is the temperature and q is the electron charge. For the calculation, the N_{cv} values from Figure 2 b) were used. So, considering N_{cv} values, PointContact device has an expected V_{oc} gain of 26 ± 10 mV over Ref. Note that this value reflects the region where this device should have the higher Na value and consequently the higher N_{cv} value. The LineContact is not expected to have a V_{oc} gain related to N_{cv}, since both PointContact and Ref devices have, within experimental variation, the same N_{cv} value and very similar Na distribution trends. In Figure 4, it demonstrated, for all devices, the V_{oc} gains that are related with the N_{cv} (ΔV_{oc}) and the V_{oc} gains that are not related with N_{cv}, which, for example, could be related with passivation effects. Moreover, it is also shown the thermodynamic losses and the V_{oc} deficit for each device. Hence, the lower V_{oc} deficit of the passivated devices compared to the Ref device cannot be fully explained by its N_{cv} value, highlighting that the lower V_{oc} deficit is likely due to the passivation effects. In Figure 4, it is not considered the V_{oc} losses in our devices that are related to: i) potential fluctuations;[84–89] ii) the used Ga profile;[52,53,90–92] iii) the lack of post deposition treatment (PDT);[93–98] and iv) the lack of a front passivation layer,[70,99–102] just to name a few potential V_{oc} losses. However, these losses should be roughly the same for the three devices.

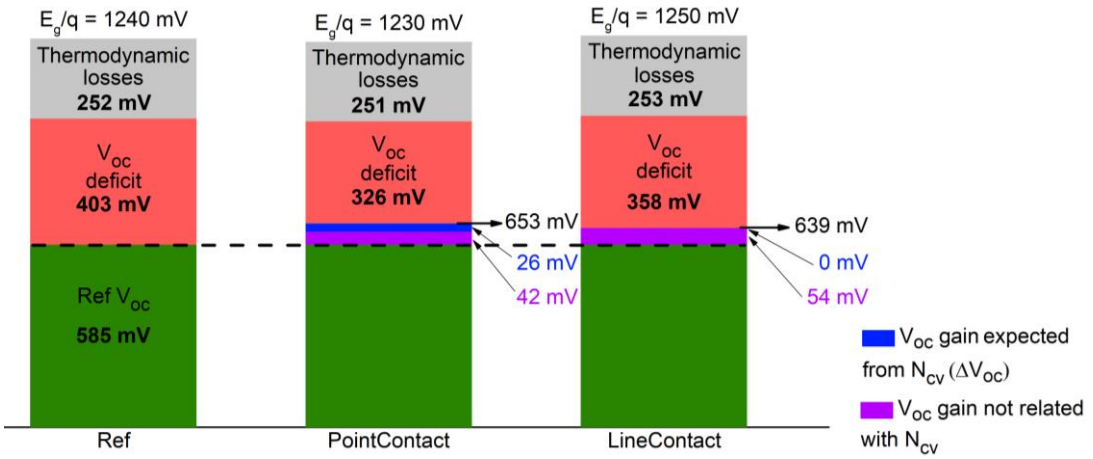

Figure 4 Passivated devices V_{oc} gains over the Ref device. The devices bandgap value is presented on top of each column. It is represented in red the V_{oc} deficit, in green the V_{oc} of the Ref device, in blue the calculated ΔV_{oc} and in purple the V_{oc} gain not related with N_{cv}. The measured V_{oc} of each device is also presented.

PointContact has a V_{oc} gain measured from J-V analysis of 68 mV over Ref, which has a difference of 42 mV compared to the calculated ΔV_{oc}. The complete V_{oc} gain is, therefore, not explained by the increased N_{cv} values. Thus, other effects, such as the passivation from the SiO_x layer are also playing a role. To further corroborate such hypothesis, one has to look to LineContact device as well. For this device, a ΔV_{oc} value of 0 mV was obtained. Nonetheless, the effective V_{oc} gain from J-V measurements was 54 mV over Ref. Therefore, the Na concentration and, consequently, the N_{cv} influence is clearly not enough to explain the V_{oc} increase seen in J-V and the chemical and/or field-effect passivation may be playing a vital role in increasing the V_{oc} values of the studied passivated devices.

Electrical simulations showed the importance to control charge density and polarity inside the insulator for optimal solar cells performance. Considering the PointContact devices' passivation area and the measured J-V figures of merit gains over the reference device, namely V_{oc} gain of 68 mV, J_{sc} gain of 1.7 mA/cm^2, same FF and efficiency gain of 1.7 %, one can infer the Q_f values present in the SiO_x layer by analyzing Figure 3. Considering such values for a passivation area of 99.7 % in Figure 3, the Q_f values inside the SiO_x insulator are negative, and they may be approximately -8x10^{12} cm^{-2}, which is an expected value for good field-effect passivation.[31,70,71] For a 59.5 % line contact passivation area and considering the observed J-

V figures of merit for this device, the same conclusions from the PointContact device may be achieved, which states that the SiO_x has a high density of negative Q_f values of approximately $-8x10^{12}$ cm^{-2}. Therefore, the Q_f values are apparently the same for both architectures, which was expected, since the Q_f is directly related with the insulator used as passivation layer, as well as, the interface with the absorber layer, which, in this case, it is also the same for both architectures. The negative charges are preferred for rear passivation and the high density of fixed charges are correlated with the increase of the field-effect passivation strength. Note that in order to accurately calculate the Q_f values present in the SiO_x layer, MIS devices will have to be fabricated with exactly the same SiO_x layer as the solar cells, but without contact holes or lines, as shown elsewhere.[30] This could be a future target. However, previous simulations have shown that the exact Q_f and surface recombination velocity (SRV) values have limited influence on the cell performances once they achieve sufficiently good values, i.e. negative Q_f and low SRV.[35] Otherwise, positive Q_f or high SRV would reduce the efficiency values of the passivated cells below the reference ones, contrarily to our observations.

The demonstrated good field-effect and/or chemical passivation effects observed by electrical simulations and J-V measurements allow SiO_x to be considered an effective choice for CIGS solar cells rear passivation.

5. Conclusions

The obtained results suggest that SiO_x deposited by the high throughput and industrial technique chemical vapor deposition is an effective insulator to be used for rear interface passivation of CIGS solar cells. Ultrathin devices with SiO_x, independently of the passivation pattern and CIGS growth temperature used, show superior optoelectronic performance compared to their respective non-passivated counterparts. The beneficial passivation effects of SiO_x allowed for an increased J-V figures of merit over the reference non-passivated device in ultrathin CIGS solar cells.

LineContact devices, that used photolithography, which is a widely used industrial technique, show promising results with a champion cell achieving a light to power conversion efficiency value of 11.7 % and an increase of the average efficiency value of 2.6 % in comparison with a non-passivated reference device. The PointContact devices, that in this work were still processed using e-beam lithography, achieved a champion cell of 12.0 %. Surprisingly, these two patterns show a compromise between V_{oc}, J_{sc} and FF connected to passivation area, and our simulations show that the studied architectures have room for further improvement, which will allow to further increase efficiency values. Therefore, the patterns shown in this work do not have ideal dimensions, as shown by the simulations, but prove that the industrially viable photolithographic device has the potential to reach the e-beam device performance. Moreover, the effects of the studied architectures for alkali introduction were discussed in the basis of GDOES measurements, highlighting the fact that a new strategy for Na introduction must be implemented. In the future, for a better understanding of this problematic, SIMS, XPS, RBS and PIXE should also be carried out together with GDOES, in order to understand the passivation layer architecture implication on the alkali distribution in the CIGS layer. Such experiments should also be strongly supported by simulations to comprehend the implications on the final solar cells devices.

The results presented here demonstrate that future improvements to the passivation pattern design can lead to even higher optoelectronical performance of the passivation structure due to a better compromise between charge extraction and passivation area demonstrating the potential of SiO_x as a passivation material for energy conversion devices. The results of this work show that widely used microelectronics processes, such as SiO_x deposited using chemical vapor deposition together with photolithography, will allow for the upscaling of the passivation layer for industrial CIGS devices. Moreover, the SiO_x layer presented here can be further used in CdTe, kesterite and perovskite solar cells, as well as, in other energy related applications, such as solid-state batteries, thermoelectrics and other devices that use complex materials.

6. Experimental

The substrates consist of 5x5 cm^2 Soda-Lime Glass (SLG) with a 350 nm layer of Mo deposited by sputtering on top of the SLG. The passivation layer fabrication procedure (Figure 5) begins by growing a SiO_x layer, 18 nm thick, by Plasma-Enhanced Chemical Vapor Deposition (PECVD) using a SPTS MPX PECVD tool at 13.56 MHz and 300 ºC. The point contact pattern is accomplished using e-beam lithography. The substrate is coated with 430 nm of polymethyl methacrylate (PMMA) resist. Then, an exposure is performed through e-beam lithography using a Vistec EBPG 5200 tool. The exposed resist is developed by methyl isobutyl ketone (MIBK) developer. Subsequently, the exposed insulator is etched by reactive ion etching (RIE) using a SPTS – ICP. The remaining resist is removed by immersing the substrates in an ultrasound bath with acetone for 30 minutes followed by a 5 minutes bath in deionized water. The accomplished pattern has a point contact structure with holes diameter of 150 nm and 2000 nm pitch.

Line contacts are patterned using photolithography where the substrate is coated with 600 nm of a positive photoresist, AZ1505. The line contact pattern is then exposed by a 405 nm laser, using a Direct Write Laser tool (Heidelberg Instruments – DWL 2000). The exposed photoresist is developed by an AZ 400K 1:4 developer. The remaining fabrication processes, etching and resist removal, followed the same conditions as the ones for the e-beam substrate. The accomplished pattern has a line contact structure with a line width of 1100 nm and 2800 nm pitch.

Regarding the used patterns, we want to point out that it is not timely and cost viable to produce lines by e-beam lithography. On the other hand, it is difficult to produce holes by photolithography with less than 1000 nm, due to the laser resolution.

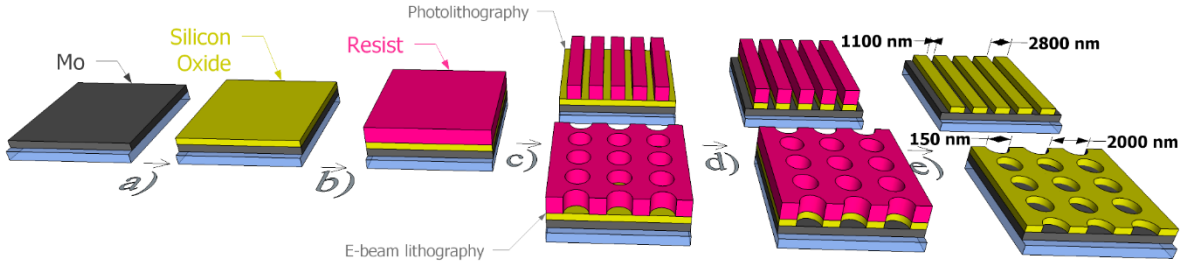

Figure 5 Photolithography and e-beam lithography step-by-step processes. The different processes are represented by: a) Insulator deposition; b) Resist coating (AZ1505 for photolithography or PMMA for e-beam lithography); c) Exposure; d) Etching; and e) Resist removal. The last image of each process has the final substrate features: photolithographic substrate with a width of 1100 nm and pitch of 2800 nm; and e-beam substrate with a width of 150 nm a pitch of 2000 nm. Images not at scale.

The 5x5 cm^2 substrates were divided in two 2.5x5 cm^2 pieces in order to grow different CIGS layers in the same substrate architecture. Prior to the CIGS layer growth, a 15 nm layer of NaF is evaporated onto all substrates. The CIGS growth is performed using a one stage co-evaporation process,[18,103,104] with a flat evaporation rate, in 2 runs: i) CIGS growth at 550 ºC, used in this work as reference CIGS growth temperature as this is the conventional temperature used,[20–22,29] with an estimated CIGS thickness of 710 nm and composition values of [Cu]/([Ga] + [In]) = 0.83 ± 0.01 and [Ga]/([Ga] + [In]) = 0.40 ± 0.02; and ii) CIGS growth at a lower temperature of 500 ºC with an estimated CIGS thickness of 710 nm and composition values of [Cu]/([Ga] + [In]) = 0.83 ± 0.01 and [Ga]/([Ga] + [In]) = 0.39 ± 0.02 as determined by X-ray fluorescence (XRF) performed in a Panalytical Epsilon 5. After growing the CIGS layer, the process follows the Ångstrom baseline.[103] The final solar cell devices are defined by scribing with an area of 0.5 cm^2. The final substrates/devices are referred according to the names present in Table 1. The reference non-passivated device is named as Ref, and passivated devices are named as PointContact or LineContact following the respective passivation architecture.

Table 1 - Names of the substrates/devices used according to the passivation architecture.

	CIGS growth temperature (ºC)	SiO_x Nanocontact Lithography
Ref	550/500	-
PointContact	550/500	E-beam
LineContact	550/500	Photolithography

A Bruker Icon Atomic Force Microscope (AFM) was used in tapping mode with a scan rate of 1 Hz for line contacts and 0.5 Hz for point contacts. Sodium compositional analyses were

performed with GDOES for in-depth profiling in combination with XRF for average in-depth composition.

Complete solar cells were characterized by AM1.5 illuminated and dark J-V, and EQE measurements performed in home-built systems. Illuminated J-V and EQE measurements were performed after light soaking at AM1.5 during 20 min with the substrate temperature being kept at 20 °C. EQE measurements were performed at 0 V bias. It is noted that the diode parameters A and J_0 were acquired from the dark curve, and the parameters R_p and R_s were acquired from the illuminated curve, according to Hegedus *et al.*.[64] The J-V figures of merit average and standard deviation values were taken from all available solar cells in each sample, which in our case are 12 solar cells. Moreover, the raw data obtained from the J-V measurements is presented in the Supporting Information together with J-V curves for all devices. The presented efficiency values were calculated using the EQE corrected J_{sc} values, which is a standard procedure for ultrathin CIGS solar cells.[10,13,20,29,104–106] C-V dark measurements were performed using a precision LCR meter Agilent E4980 A with a 10 kHz frequency signal and a V_{RMS} of 25 mV. The bias applied ranged from -0.5 V to 0.7 V. For the C-V measurements, all 12 cells were measured and the data obtained from the N_{cv} and *W* analyses is presented in the Supporting Information together with N_{cv}-*W* curves for all devices. Atypical cells were removed.

The presented plots for each measurement always have in consideration a representative solar cell, and the choice is based on the average measurement value, i.e. the solar cell with the studied parameter closer to its average value is considered to be the representative one.

The electrical properties of a 710 nm thick CIGS device were simulated using the Silvaco ATLAS 2D program, as specified elsewhere.[35] The crucial parameters used were contact resistance (R_c), bulk defect density, rear reflectance (R_b), doping density and SRV at the rear interface. In order to approach reality, the SRV value has been differentiated for the two rear interfaces Mo/CIGS and SiO_x/CIGS. All the used parameter values are listed in Table 2. The default R_c value of 0.1 $\Omega.cm^2$ used for the passivated devices represents an equivalent series

resistance of 1 $\Omega.cm^2$ in our 2D model, identical to the reference device, as described elsewhere.[35] The R_c value accounts for the resistance in the nanocontact openings for the passivated devices, scaled by the width to pitch ratio of the opening,[35] i.e. assuming by default an average width to pitch ratio of 0.1 as the same for both structures. The presented defect density is related to bulk mid-gap acceptor defects.[35] The chosen R_b values were based on optical simulations,[35] whereas the doping density values were based on experimental data.[35] The simulations were conducted assuming the pitch value of 2000 and 2800 nm as obtained in the experiments. Nonetheless, since similar results were obtained, only simulations with a pitch value of 2000 nm were presented and analyzed.

Table 2 Crucial parameter values used in Silvaco ATLAS 2D electrical simulations. It is noted that for the passivated devices, it is represented the SRV value inside the nanocontacts (Mo/CIGS) and outside the nanocontacts (SiO_x/CIGS).

	R_c ($\Omega.cm^2$)	Defect density (cm^{-3})	R_b (%)	Doping density (cm^{-3})	SRV (cm/s)
Ref	1	2×10^{14}	20	3×10^{16}	Mo/CIGS 1×10^{7}
PointContact	0.1	1×10^{14}	45	5×10^{16}	Mo/CIGS 1×10^{7} SiO_x/CIGS 1×10^{2}
LineContact	0.1	1×10^{14}	45	5×10^{16}	Mo/CIGS 1×10^{7} SiO_x/CIGS 1×10^{2}

6.1 | Passivation structure

AFM topography images were taken from all fabricated substrates. Figures 6 a) and b) show representative 3D AFM images of point and line contact substrates, respectively, showing well-defined vertical features for both cases. Figures 6 c) and d) show the AFM cross-section representative plot of a contact opening for each type of substrate architecture, from which the average value of the contact width was estimated (Figure 6 e)). In the cross-section plot, the double red arrow represents the average contact width, and it is established by considering the complete removal of the SiO_x layer with an 18 nm thickness.

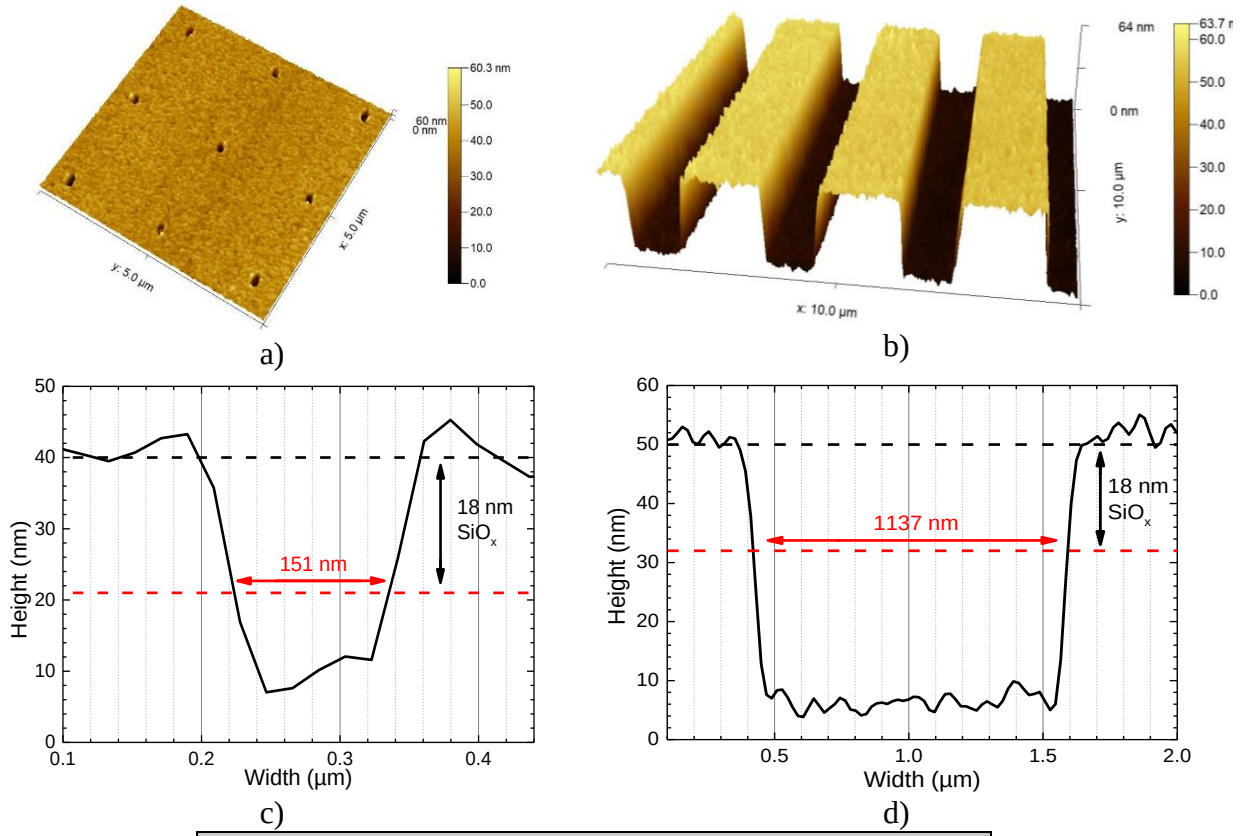

e)	Passivation area (%)	Contact width (nm)
PointContact	99.7	151 ± 22
LineContact	59.5	1137 ± 13

Figure 6 Representative AFM 3D image of: a) point contact; and b) line contact based substrates. Representative AFM cross-section plot of: c) point contact; d) line contact based substrates, where it is shown the SiO_x thickness (double black arrow) and the average contact width (double red arrow); and e) Contact width average and standard deviation values of both studied substrate architectures. Average values were taken in 9 patterns of the same AFM image. The passivation area for each device is also presented. Representative AFM images of the substrates were chosen based on the contact width value closer to the average contact width value.

The PointContact substrate resulted in contacts with an equivalent diameter average value of 151 nm, and the LineContact substrates resulted in line contacts with an average width value of 1137 nm. Average values were taken in 9 patterns of the same AFM image. Therefore, according to equations (1) and (2), the PointContact substrate resulted in a 99.7 % of passivated area, whereas the LineContact architecture allows for a 59.5 % of passivated area, as summarized in Figure 6 e).

Supporting Information

Supporting Information is available from the Wiley Online Library or from the author.

ACKNOWLEDGEMENTS

Fundação para a Ciência e a Tecnologia (FCT) is acknowledged through the project IF/00133/2015, PD/BD/142780/2018, SFRH/BD/146776/2019 and UIDB/04730/2020. The

European Union's Horizon 2020 research and innovation programme ARCIGS-M project (grant agreement no. 720887) is acknowledged. This research is also supported by NovaCell – Development of novel Ultrathin Solar Cell Architectures for low-light, low-cost, and flexible opto-electronic devices project (028075) co-funded by FCT and the ERDF through COMPETE2020. This research is supported by InovSolarCells – Development of innovative nanostructured dielectric materials for interface passivation in thin film solar cells project (029696) co-funded by FCT and the ERDF through COMPETE2020.

Received: ((will be filled in by the editorial staff))
Revised: ((will be filled in by the editorial staff))
Published online: ((will be filled in by the editorial staff))

REFERENCES

[1] I. S. E. Fraunhofer Institute for Solar Energy Systems, PSE Projects GmbH, *Photovoltaics Report*; 2020.

[2] M. A. Green, E. D. Dunlop, J. Hohl-Ebinger, M. Yoshita, N. Kopidakis, A. W. Y. Ho-Baillie, *Prog. Photovoltaics Res. Appl.* **2020**, *28*, 3.

[3] M. Nakamura, K. Yamaguchi, Y. Kimoto, Y. Yasaki, T. Kato, H. Sugimoto, *IEEE J. Photovoltaics* **2019**, *9*, 1863.

[4] B. Vermang, J. T. Watjen, C. Frisk, V. Fjallstrom, F. Rostvall, M. Edoff, P. M. P. Salomé, J. Borme, N. Nicoara, S. Sadewasser, *IEEE J. Photovoltaics* **2014**, *4*, 1644.

[5] L. M. Mansfield, A. Kanevce, S. P. Harvey, K. Bowers, C. Beall, S. Glynn, I. L. Repins, *Prog. Photovoltaics Res. Appl.* **2018**, *26*, 949.

[6] S. Yang, J. Zhu, X. Zhang, X. Ma, H. Luo, L. Yin, X. Xiao, *Prog. Photovoltaics Res. Appl.* **2015**, *23*, 1157.

[7] V. Fthenakis, *Renew. Sustain. Energy Rev.* **2009**, *13*, 2746.

[8] D. Kim, S. S. Shin, S. M. Lee, J. Cho, J. H. Yun, H. S. Lee, J. H. Park, *Adv. Funct. Mater.* **2020**, 2001775.

[9] L. Stamford, A. Azapagic, *Sci. Total Environ.* **2019**, *688*, 1092.

[10] O. Lundberg, M. Bodegård, J. Malmström, L. Stolt, *Prog. Photovoltaics Res. Appl.* **2003**, *11*, 77.

[11] A. Duchatelet, E. Letty, S. Jaime-Ferrer, P.-P. Grand, F. Mollica, N. Naghavi, *Sol. Energy Mater. Sol. Cells* **2017**, *162*, 114.

[12] S.-U. Park, R. Sharma, J.-K. Sim, B. J. Baek, H.-K. Ahn, J. S. Kim, C.-R. Lee, *Appl. Surf. Sci.* **2013**,

280, 757.

[13] C. van Lare, G. Yin, A. Polman, M. Schmid, *ACS Nano* **2015**, *9*, 9603.

[14] M. Schmid, *Semicond. Sci. Technol.* **2017**, *32*, 043003.

[15] G. Yin, P. Manley, M. Schmid, *Sol. Energy* **2018**, *163*, 443.

[16] A. J. N. Oliveira, J. de Wild, K. Oliveira, B. A. Valença, J. P. Teixeira, J. R. L. Guerreiro, S. Abalde-Cela, T. S. Lopes, R. M. Ribeiro, J. M. V. Cunha, M. A. Curado, M. Monteiro, A. Violas, A. G. Silva, M. Prado, P. A. Fernandes, B. Vermang, P. M. P. Salomé, *Sol. RRL* **2020**, *4*, 2000310.

[17] R. Brendel, H. J. Queisser, *Sol. Energy Mater. Sol. Cells* **1993**, *29*, 397.

[18] P. M. P. Salomé, B. Vermang, R. Ribeiro-Andrade, J. P. Teixeira, J. M. V. Cunha, M. J. Mendes, S. Haque, J. Borme, H. Águas, E. Fortunato, R. Martins, J. C. González, J. P. Leitão, P. A. Fernandes, M. Edoff, S. Sadewasser, *Adv. Mater. Interfaces* **2018**, *5*, 1701101.

[19] S. Bose, J. M. V. Cunha, J. Borme, W. C. Chen, N. S. Nilsson, J. P. Teixeira, J. Gaspar, J. P. Leitão, M. Edoff, P. A. Fernandes, P. M. P. Salomé, *Thin Solid Films* **2019**, *671*, 77.

[20] S. Bose, J. M. V. Cunha, S. Suresh, J. De Wild, T. S. Lopes, J. R. S. Barbosa, R. Silva, J. Borme, P. A. Fernandes, B. Vermang, P. M. P. Salomé, *Sol. RRL* **2018**, *2*, 1800212.

[21] T. S. Lopes, J. M. V. Cunha, S. Bose, J. R. Barbosa, J. Borme, O. Donzel-Gargand, C. Rocha, R. Silva, A. Hultqvist, W.-C. Chen, A. G. Silva, M. Edoff, P. A. Fernandes, P. M. P. Salomé, *IEEE J. Photovoltaics* **2019**, *9*, 1421.

[22] J. M. V. Cunha, T. S. Lopes, S. Bose, A. Hultqvist, W.-C. Chen, O. Donzel-Gargand, R. M. Ribeiro, A. J. N. Oliveira, M. Edoff, P. A. Fernandes, P. M. P. Salomé, *IEEE J. Photovoltaics* **2019**, *9*, 1857.

[23] B. Vermang, J. T. Wätjen, V. Fjällström, F. Rostvall, M. Edoff, R. Kotipalli, F. Henry, D. Flandre, *Prog. Photovoltaics Res. Appl.* **2014**, *22*, 1023.

[24] B. Vermang, V. Fjallstrom, X. Gao, M. Edoff, *IEEE J. Photovoltaics* **2014**, *4*, 486.

[25] G. Birant, J. de Wild, M. Meuris, J. Poortmans, B. Vermang, *Appl. Sci.* **2019**, *9*, 677.

[26] G. Yin, M. Song, S. Duan, P. Manley, D. Greiner, C. A. Kaufmann, M. Schmid, *ACS Appl. Mater. Interfaces* **2016**, *8*, 31646.

[27] E. Jarzembowski, B. Fuhrmann, H. Leipner, W. Fränzel, R. Scheer, *Thin Solid Films* **2017**, *633*, 61.

[28] C. Chen, H. Tsai, Y. Wang, Y. Shih, T. Su, C. Yang, W. Lin, C. Shen, J. Shieh, Y. Chueh, *Adv. Funct. Mater.* **2019**, *29*, 1905040.

[29] D. Ledinek, P. M. P. Salomé, C. Hagglund, U. Zimmermann, M. Edoff, *IEEE J. Photovoltaics* **2018**, *8*, 864.

[30] J. M. V. Cunha, P. A. Fernandes, A. Hultqvist, J. P. Teixeira, S. Bose, B. Vermang, S. Garud, D. Buldu, J. Gaspar, M. Edoff, J. P. Leitão, P. M. P. Salomé, *IEEE J. Photovoltaics* **2018**, *8*, 1313.

[31] R. Kotipalli, B. Vermang, J. Joel, R. Rajkumar, M. Edoff, D. Flandre, *AIP Adv.* **2015**, *5*, 107101.

[32] F. Mollica, J. Goffard, M. Jubault, F. Donsanti, S. Collin, A. Cattoni, L. Lombez, N. Naghavi, In *2016 IEEE 43rd Photovoltaic Specialists Conference (PVSC)*; IEEE, 2016; pp. 2213–2217.

[33] J. M. V. Cunha, C. Rocha, C. Vinhais, P. A. Fernandes, P. M. P. Salomé, *IEEE J. Photovoltaics* **2019**, *9*, 1442.

[34] G. Yin, M. Song, M. Schmid, *Sol. Energy Mater. Sol. Cells* **2019**, *195*, 318.

[35] J. Lontchi, M. Zhukova, M. Kovacic, J. Krc, W.-C. Chen, M. Edoff, S. Bose, P. M. P. Salome, J. Goffard, A. Cattoni, L. Gouillart, S. Collin, V. Gusak, D. Flandre, *IEEE J. Photovoltaics* **2020**, *10*, 1908.

[36] J. M. Kephart, A. Kindvall, D. Williams, D. Kuciauskas, P. Dippo, A. Munshi, W. S. Sampath, *IEEE J. Photovoltaics* **2018**, *8*, 587.

[37] D. Kuciauskas, J. M. Kephart, J. Moseley, W. K. Metzger, W. S. Sampath, P. Dippo, *Appl. Phys. Lett.* **2018**, *112*, 263901.

[38] B. Vermang, Y. Ren, O. Donzel-Gargand, C. Frisk, J. Joel, P. Salome, J. Borme, S. Sadewasser, C. Platzer-Bjorkman, M. Edoff, *IEEE J. Photovoltaics* **2016**, *6*, 332.

[39] J. Liang, Q. Lin, H. Li, Y. Su, X. Yang, Z. Wu, J. Zheng, X. Wang, Y. Lin, F. Pan, *Appl. Phys. Lett.* **2015**, *107*, 013907.

[40] A. Krishna, M. A. Akhavan Kazemi, M. Sliwa, G. N. M. Reddy, L. Delevoye, O. Lafon, A. Felten, M. T. Do, S. Gottis, F. Sauvage, *Adv. Funct. Mater.* **2020**, *30*, 1909737.

[41] Q. Jiang, Y. Zhao, X. Zhang, X. Yang, Y. Chen, Z. Chu, Q. Ye, X. Li, Z. Yin, J. You, *Nat. Photonics* **2019**, *13*, 460.

[42] Y. H. Lee, J. Luo, M.-K. Son, P. Gao, K. T. Cho, J. Seo, S. M. Zakeeruddin, M. Grätzel, M. K. Nazeeruddin, *Adv. Mater.* **2016**, *28*, 3966.

[43] H. Zhang, Y. Wu, C. Shen, E. Li, C. Yan, W. Zhang, H. Tian, L. Han, W. Zhu, *Adv. Energy Mater.* **2019**, *9*, 1803573.

[44] S. Akin, N. Arora, S. M. Zakeeruddin, M. Grätzel, R. H. Friend, M. I. Dar, *Adv. Energy Mater.* **2020**, *10*, 1903090.

[45] F. Gao, Y. Zhao, X. Zhang, J. You, *Adv. Energy Mater.* **2020**, *10*, 1902650.

[46] Y. S. Lee, T. Gershon, T. K. Todorov, W. Wang, M. T. Winkler, M. Hopstaken, O. Gunawan, J. Kim, *Adv. Energy Mater.* **2016**, *6*, 1600198.

[47] P. D. Antunez, D. M. Bishop, Y. S. Lee, T. Gokmen, O. Gunawan, T. S. Gershon, T. K. Todorov, S. Singh, R. Haight, *Adv. Energy Mater.* **2017**, *7*, 1602585.

[48] K. Prabhakaran, F. Maeda, Y. Watanabe, T. Ogino, *Thin Solid Films* **2000**, *369*, 289.

[49] D. Rudmann, D. Brémaud, A. F. da Cunha, G. Bilger, A. Strohm, M. Kaelin, H. Zogg, A. N. Tiwari, *Thin Solid Films* **2005**, *480–481*, 55.

[50] L. Zhang, Q. He, W.-L. Jiang, F.-F. Liu, C.-J. Li, Y. Sun, *Sol. Energy Mater. Sol. Cells* **2009**, *93*, 114.

[51] G. Sozzi, F. Troni, R. Menozzi, *Proc. CS-ManTech* **2010**, 353.

[52] P. M. P. Salomé, A. Hultqvist, V. Fjällström, B. Vermang, M. Edoff, B. Aitken, K. Zhang, K. Fuller, C. Kosik Williams, *Sol. Energy Mater. Sol. Cells* **2014**, *123*, 166.

[53] J. Haarstrich, H. Metzner, M. Oertel, C. Ronning, T. Rissom, C. A. Kaufmann, T. Unold, H. W. Schock, J. Windeln, W. Mannstadt, E. Rudigier-Voigt, *Sol. Energy Mater. Sol. Cells* **2011**, *95*, 1028.

[54] P. M. P. Salomé, H. Rodriguez-Alvarez, S. Sadewasser, *Sol. Energy Mater. Sol. Cells* **2015**, *143*, 9.

[55] P. M. P. Salomé, A. Hultqvist, V. Fjällström, M. Edoff, B. Aitken, K. Vaidyanathan, K. Zhang, K. Fuller, C. Kosik Williams, *IEEE J. Photovoltaics* **2013**, *3*, 852.

[56] S. Puttnins, S. Levcenco, K. Schwarzburg, G. Benndorf, F. Daume, A. Rahm, A. Braun, M. Grundmann, T. Unold, *Sol. Energy Mater. Sol. Cells* **2013**, *119*, 281.

[57] D. Rudmann, A. F. da Cunha, M. Kaelin, F. Kurdesau, H. Zogg, A. N. Tiwari, G. Bilger, *Appl. Phys. Lett.* **2004**, *84*, 1129.

[58] R. Scheer, H.-W. Schock, *Chalcogenide photovoltaics: physics, technologies, and thin film devices*; John Wiley & Sons, 2011.

[59] A. Niemegeers, M. Burgelman, R. Herberholz, U. Rau, D. Hariskos, H.-W. Schock, *Prog. Photovoltaics Res. Appl.* **1998**, *6*, 407.

[60] R. Klenk, *Thin Solid Films* **2001**, *387*, 135.

[61] P. M. P. Salomé, V. Fjällström, A. Hultqvist, M. Edoff, *IEEE J. Photovoltaics* **2013**, *3*, 509.

[62] R. Caballero, C. A. Kaufmann, T. Eisenbarth, A. Grimm, I. Lauermann, T. Unold, R. Klenk, H. W. Schock, *Appl. Phys. Lett.* **2010**, *96*, 092104.

[63] W. N. Sharaman, R. W. Birkmire, S. Marsillac, M. Marudachalam, N. Orbey, T. W. F. Russell, In *Conference Record of the Twenty Sixth IEEE Photovoltaic Specialists Conference-1997*; IEEE, 1997; pp. 331–334.

[64] S. S. Hegedus, W. N. Shafarman, *Prog. Photovoltaics Res. Appl.* **2004**, *12*, 155.

[65] U. Malm, J. Malmström, C. Platzer-Björkman, L. Stolt, *Thin Solid Films* **2005**, *480–481*, 208.

[66] M. Cwil, M. Igalson, P. Zabierowski, S. Siebentritt, *J. Appl. Phys.* **2008**, *103*, 063701.

[67] P. M. P. Salomé, J. Keller, T. Törndahl, J. P. Teixeira, N. Nicoara, R.-R. Andrade, D. G. Stroppa, J. C. González, M. Edoff, J. P. Leitão, S. Sadewasser, *Sol. Energy Mater. Sol. Cells* **2017**, *159*, 272.

[68] P. M. P. Salomé, V. Fjallstrom, A. Hultqvist, P. Szaniawski, U. Zimmermann, M. Edoff, *Prog. Photovoltaics Res. Appl.* **2014**, *22*, 83.

[69] D. J. Schroeder, A. A. Rockett, *J. Appl. Phys.* **1997**, *82*, 4982.

[70] G. Sozzi, S. Di Napoli, R. Menozzi, B. Bissig, S. Buecheler, A. N. Tiwari, *Sol. Energy Mater. Sol. Cells* **2017**, *165*, 94.

[71] R. Kotipalli, O. Poncelet, G. Li, Y. Zeng, L. A. Francis, B. Vermang, D. Flandre, *Sol. Energy* **2017**, *157*, 603.

[72] A. Wolf, D. Biro, J. Nekarda, S. Stumpp, A. Kimmerle, S. Mack, R. Preu, *J. Appl. Phys.* **2010**, *108*, 124510.

[73] M. Edoff, T. Jarmar, N. S. Nilsson, E. Wallin, D. Hogstrom, O. Stolt, O. Lundberg, W. Shafarman, L. Stolt, *IEEE J. Photovoltaics* **2017**, *7*, 1789.

[74] A. G. Karydas, I. Bogdanovic Radovic, C. Streeck, C. Kaufmann, R. Caballero, T. Rissom, B. Kanngießer, B. Beckhoff, M. Jaksic, N. P. Barradas, *Nucl. Instruments Methods Phys. Res. Sect. B Beam Interact. with Mater. Atoms* **2014**, *331*, 93.

[75] D. Spemann, K. Otte, M. Lorenz, T. Butz, *Nucl. Instruments Methods Phys. Res. Sect. B Beam Interact. with Mater. Atoms* **2005**, *231*, 440.

[76] R. Wuerz, A. Eicke, M. Frankenfeld, F. Kessler, M. Powalla, P. Rogin, O. Yazdani-Assl, *Thin Solid Films* **2009**, *517*, 2415.

[77] W. C. Lim, J. Lee, S. Won, Y. Lee, *Surf. Interface Anal.* **2012**, *44*, 724.

[78] M. A. Curado, J. P. Teixeira, M. Monteiro, E. F. M. Ribeiro, R. C. Vilão, H. V. Alberto, J. M. V. Cunha, T. S. Lopes, K. Oliveira, O. Donzel-Gargand, A. Hultqvist, S. Calderon, M. A. Barreiros, W. Chiappim, J. P. Leitão, A. G. Silva, T. Prokscha, C. Vinhais, P. A. Fernandes, P. M. P. Salomé, *Appl. Mater. Today* **2020**, *21*, 100867.

[79] S. Lany, A. Zunger, *J. Appl. Phys.* **2006**, *100*, 113725.

[80] A. Urbaniak, M. Igalson, *J. Appl. Phys.* **2009**, *106*, 063720.

[81] S. Siebentritt, T. Rissom, *Appl. Phys. Lett.* **2008**, *92*, 062107.

[82] F. Pianezzi, P. Reinhard, A. Chirilă, B. Bissig, S. Nishiwaki, S. Buecheler, A. N. Tiwari, *Phys. Chem. Chem. Phys.* **2014**, *16*, 8843.

[83] S. Karki, S. Marsillac, P. Paul, G. Rajan, B. Belfore, D. Poudel, A. Rockett, E. Danilov, F. Castellano, A. Arehart, *IEEE J. Photovoltaics* **2019**, *9*, 313.

[84] J. P. Teixeira, P. M. P. Salomé, B. Alves, M. Edoff, J. P. Leitão, *Phys. Rev. Appl.* **2019**, *11*, 054013.

[85] A. Nikolaeva, M. Krause, N. Schäfer, W. Witte, D. Hariskos, T. Kodalle, C. A. Kaufmann, N. Barreau, D. Abou-Ras, *Prog. Photovoltaics Res. Appl.* **2020**, pip. 3299.

[86] J. H. Werner, J. Mattheis, U. Rau, *Thin Solid Films* **2005**, *480–481*, 399.

[87] S. Siebentritt, *Sol. Energy Mater. Sol. Cells* **2011**, *95*, 1471.

[88] J. Mattheis, U. Rau, J. H. Werner, *J. Appl. Phys.* **2007**, *101*, 113519.

[89] D. Abou-Ras, N. Schäfer, C. J. Hages, S. Levcenko, J. Márquez, T. Unold, *Sol. RRL* **2018**, *2*, 1700199.

[90] J. P. Teixeira, R. B. L. Vieira, B. P. Falcão, M. Edoff, P. M. P. Salomé, J. P. Leitão, *J. Phys. Chem. C* **2020**, *124*, 12295.

[91] J. Song, S. S. Li, C. H. Huang, O. D. Crisalle, T. J. Anderson, *Solid. State. Electron.* **2004**, *48*, 73.

[92] O. Lundberg, M. Edoff, L. Stolt, *Thin Solid Films* **2005**, *480–481*, 520.

[93] T. S. Lopes, J. de Wild, C. Rocha, A. Violas, J. M. V. Cunha, J. P. Teixeira, M. A. Curado, A. J. N. Oliveira, J. Borme, G. Birant, G. Brammertz, P. A. Fernandes, B. Vermang, P. M. P. Salomé, *Submited to ACS Applied Materials & Interfaces*.

[94] P. Reinhard, F. Pianezzi, B. Bissig, A. Chirila, P. Blosch, S. Nishiwaki, S. Buecheler, A. N. Tiwari, *IEEE J. Photovoltaics* **2015**, *5*, 656.

[95] S. A. Jensen, S. Glynn, A. Kanevce, P. Dippo, J. V. Li, D. H. Levi, D. Kuciauskas, *J. Appl. Phys.* **2016**, *120*, 063106.

[96] S. Siebentritt, E. Avancini, M. Bär, J. Bombsch, E. Bourgeois, S. Buecheler, R. Carron, C. Castro, S. Duguay, R. Félix, E. Handick, D. Hariskos, V. Havu, P. Jackson, H. Komsa, T. Kunze, M. Malitckaya, R. Menozzi, M. Nesladek, N. Nicoara, M. Puska, M. Raghuwanshi, P. Pareige, S. Sadewasser, G. Sozzi, A. N. Tiwari, S. Ueda, A. Vilalta-Clemente, T. P. Weiss, F. Werner, R. G. Wilks, W. Witte, M. H. Wolter, *Adv. Energy Mater.* **2020**, *10*, 1903752.

[97] P. Jackson, D. Hariskos, R. Wuerz, W. Wischmann, M. Powalla, *Phys. status solidi - Rapid Res. Lett.* **2014**, *8*, 219.

[98] R. Kamada, T. Yagioka, S. Adachi, A. Handa, K. F. Tai, T. Kato, H. Sugimoto, In *2016 IEEE 43rd Photovoltaic Specialists Conference (PVSC)*; IEEE, 2016; pp. 1287–1291.

[99] S. Garud, N. Gampa, T. G. Allen, R. Kotipalli, D. Flandre, M. Batuk, J. Hadermann, M. Meuris, J. Poortmans, A. Smets, B. Vermang, *Phys. status solidi* **2018**, *215*, 1700826.

[100] F. Werner, B. Veith-Wolf, M. Melchiorre, F. Babbe, J. Schmidt, S. Siebentritt, *Sci. Rep.* **2020**, *10*, 7530.

[101] P. Reinhard, B. Bissig, F. Pianezzi, H. Hagendorfer, G. Sozzi, R. Menozzi, C. Gretener, S. Nishiwaki, S. Buecheler, A. N. Tiwari, *Nano Lett.* **2015**, *15*, 3334.

[102] G. Sozzi, D. Pignoloni, R. Menozzi, F. Pianezzi, P. Reinhard, B. Bissig, S. Buecheler, A. N. Tiwari, In *2015 IEEE 42nd Photovoltaic Specialist Conference (PVSC)*; IEEE, 2015; pp. 1–5.

[103] J. Lindahl, U. Zimmermann, P. Szaniawski, T. Torndahl, A. Hultqvist, P. M. P. Salomé, C. Platzer-Bjorkman, M. Edoff, *IEEE J. Photovoltaics* **2013**, *3*, 1100.

[104] D. Ledinek, J. Keller, C. Hägglund, W.-C. Chen, M. Edoff, *Thin Solid Films* **2019**, *683*, 156.

[105] L. Gouillart, S. Collin, W.-C. Chen, A. Cattoni, J. Goffard, L. Riekehr, J. Keller, M. Jubault, N. Naghavi, M. Edoff, *IEEE J. Photovoltaics* **2020**, *10*, 250.

[106] L. Gouillart, A. Cattoni, J. Goffard, F. Donsanti, G. Patriarche, M. Jubault, N. Naghavi, S. Collin, *Thin Solid Films* **2019**, *672*, 1.

List of figures

a)	CIGS growth temperature (°C)	V_{oc} (mV)	EQE corrected J_{sc} (mA/cm²)	FF (%)	Eff. (%)
Ref	550	585 ± 7 (597)	22.50 ± 0.44 (22.72)	66.9 ± 1.3 (69.8)	8.8 ± 0.4 (9.5)
PointContact	550	653 ± 13 (673)	24.23 ± 0.67 (24.77)	66.6 ± 2.6 (71.9)	10.5 ± 0.7 (12.0)
LineContact	550	639 ± 7 (652)	23.80 ± 0.21 (23.55)	74.7 ± 0.8 (76.4)	11.4 ± 0.2 (11.7)
Ref	500	523 ± 14 (537)	23.67 ± 0.85 (25.25)	50.2 ± 8.8 (60.8)	6.2 ± 1.3 (8.2)
PointContact	500	614 ± 21 (657)	23.99 ± 0.56 (25.16)	55.6 ± 3.2 (63.4)	8.2 ± 0.9 (10.5)
LineContact	500	588 ± 9 (600)	23.97 ± 0.45 (25.04)	65.9 ± 1.9 (69.2)	9.3 ± 0.5 (10.4)

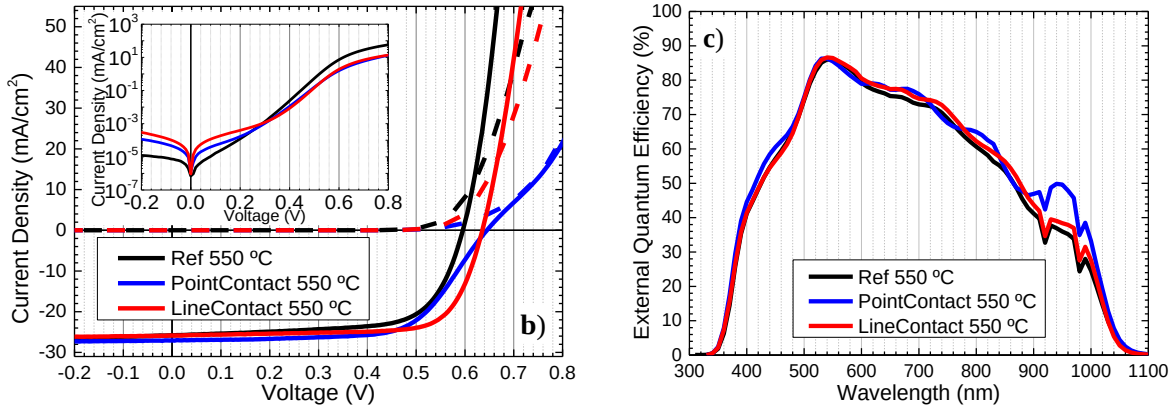

d)	R_p (Ω.cm²)	R_s (Ω.cm²)	A	J_0 (mA/cm²)
Ref	326 ± 47	0.68 ± 0.06	1.25	(43.6 ± 10.1) x10^{-8}
PointContact	1573 ± 406	1.28 ± 0.18	1.45	(25.0 ± 12.3) x10^{-8}
LineContact	754 ± 95	0.66 ± 0.04	1.35	(6.97 ± 1.16) x10^{-8}

Figure 1 a) J-V figures of merit: averages and standard deviations values of all studied devices. Figures of merit values for the highest efficiency cells also presented in brackets. J_{sc} values calculated from the EQE spectra. Averages taken from 12 cells; b) Representative J-V plots of the device with the efficiency value closer to the efficiency average value. Straight lines are illuminated curves and dashed lines are dark curves. The inset figure is the dark log J-V curve; c) Representative EQE plots of the device with the J_{sc} value closer to the J_{sc} average value; and d) Solar cells' diode parameters average and standard deviation values for devices grown with a substrate temperature of 550 ºC. R_p stands for parallel resistance, R_s for series resistance, A for ideality factor and J_0 for saturation current density.

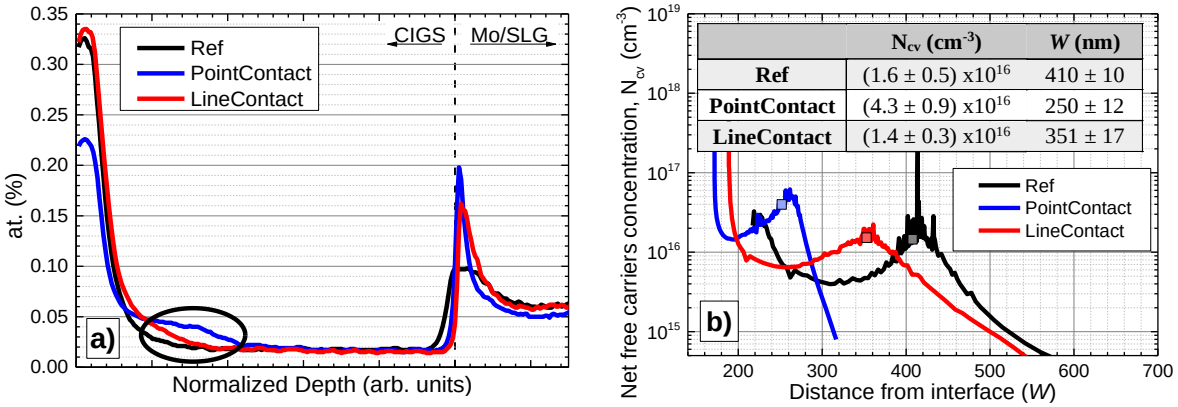

	N_{cv} (cm^{-3})	W (nm)
Ref	(1.6 ± 0.5) x10^{16}	410 ± 10
PointContact	(4.3 ± 0.9) x10^{16}	250 ± 12
LineContact	(1.4 ± 0.3) x10^{16}	351 ± 17

Figure 2 a) GDOES Na in-depth profile of devices grown with a substrate temperature of 550 ºC. The dashed vertical line is a guide to the eye representing where the CIGS/Mo interface is located; and b) Representative N_{cv} vs W plot of the device with the N_{cv} and W values closer to the N_{cv} and W average values. The depletion region and net free carrier concentration are taken at 0 V and are represented in square marks. Inset table represents the zero-bias average and standard deviation values of N_{cv} and W. Averages taken from 12 cells.

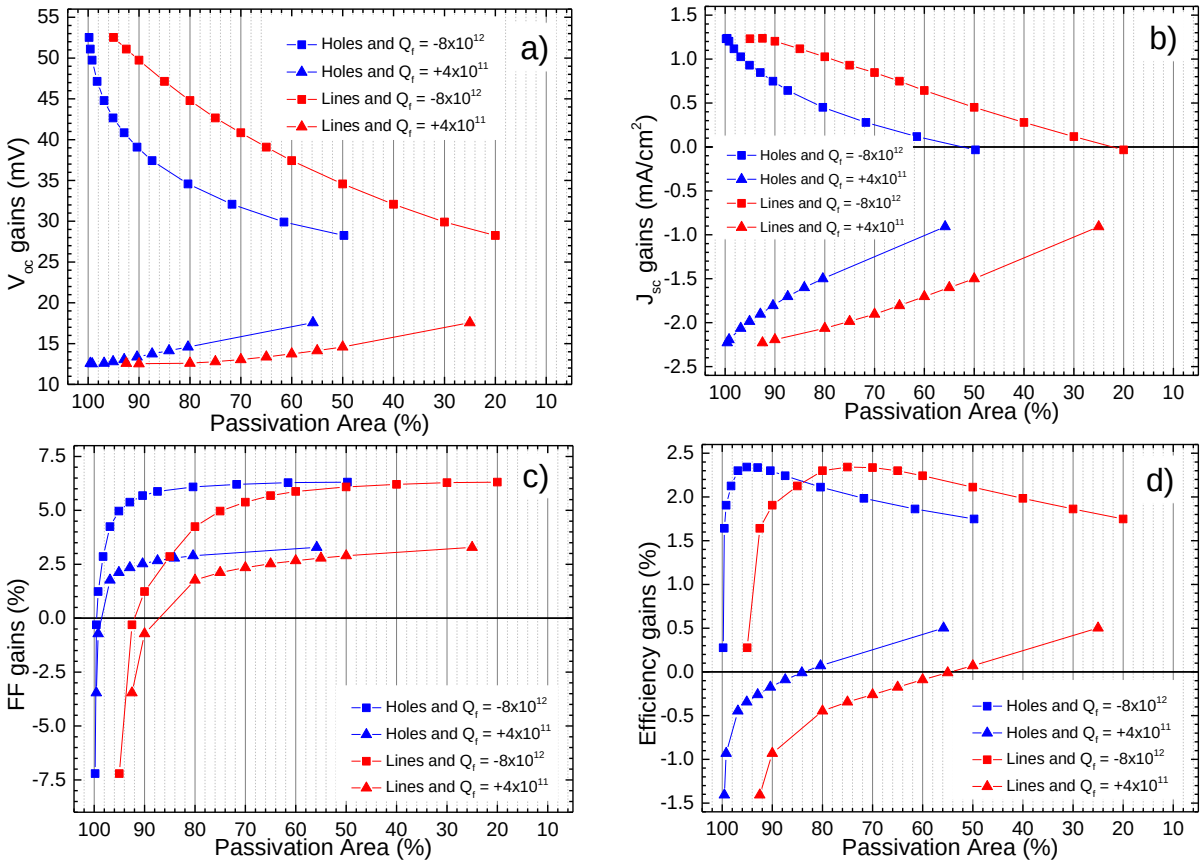

Figure 3 - Figures of merit absolute gains of the passivated devices over the reference device: a) V_{oc} gains; b) J_{sc} gains; c) FF gains; and d) Efficiency gains. Pitch value of 2000 nm simulated. Red lines correspond to the passivation area for line contacts and blue lines correspond to the passivation area for point contacts. Square marks represent a Q_f value of $-8x10^{12}$ cm^{-2} and triangle marks represent a Q_f value of $+4x10^{11}$ cm^{-2}.

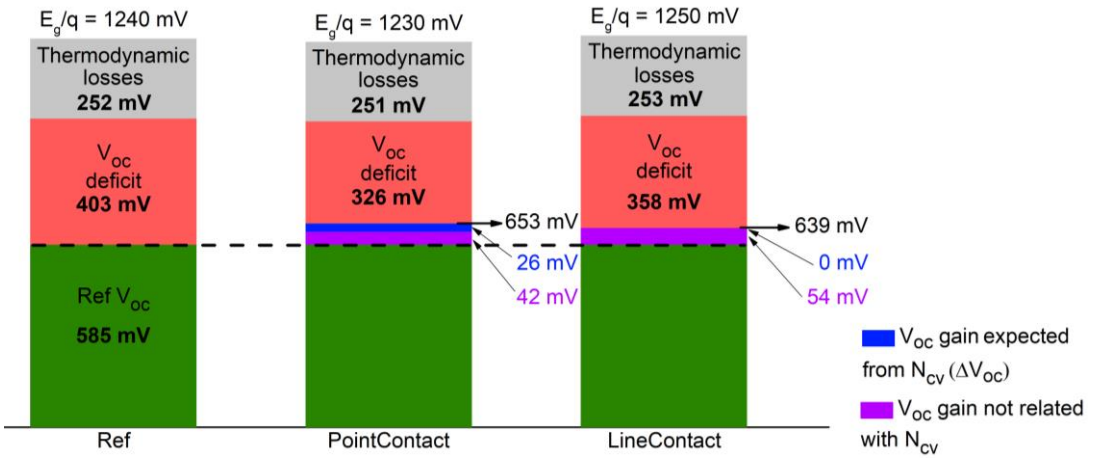

Figure 4 Passivated devices V_{oc} gains over the Ref device. The devices bandgap value is presented on top of each column. It is represented in red the V_{oc} deficit, in green the V_{oc} of the Ref device, in blue the calculated ΔV_{oc} and in purple the V_{oc} gain not related with N_{cv}. The measured V_{oc} of each device is also presented.

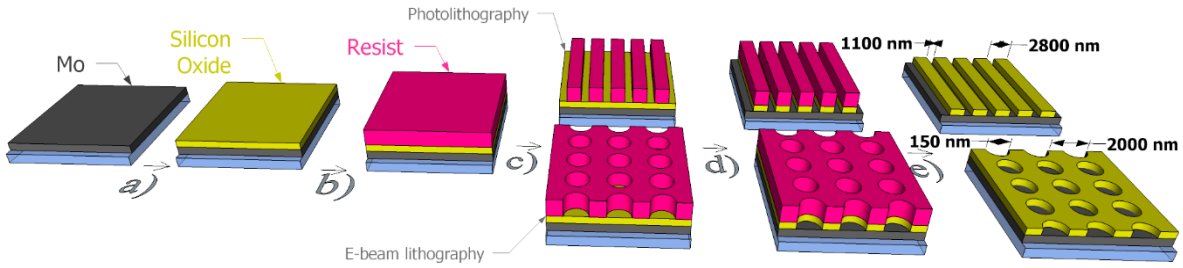

Figure 5 Photolithography and e-beam lithography step-by-step processes. The different processes are represented by: a) Insulator deposition; b) Resist coating (AZ1505 for photolithography or PMMA for e-beam lithography); c) Exposure; d) Etching; and e) Resist removal. The last image of each process has the final substrate features: photolithographic substrate with a width of 1100 nm and pitch of 2800 nm; and e-beam substrate with a width of 150 nm a pitch of 2000 nm. Images not at scale.

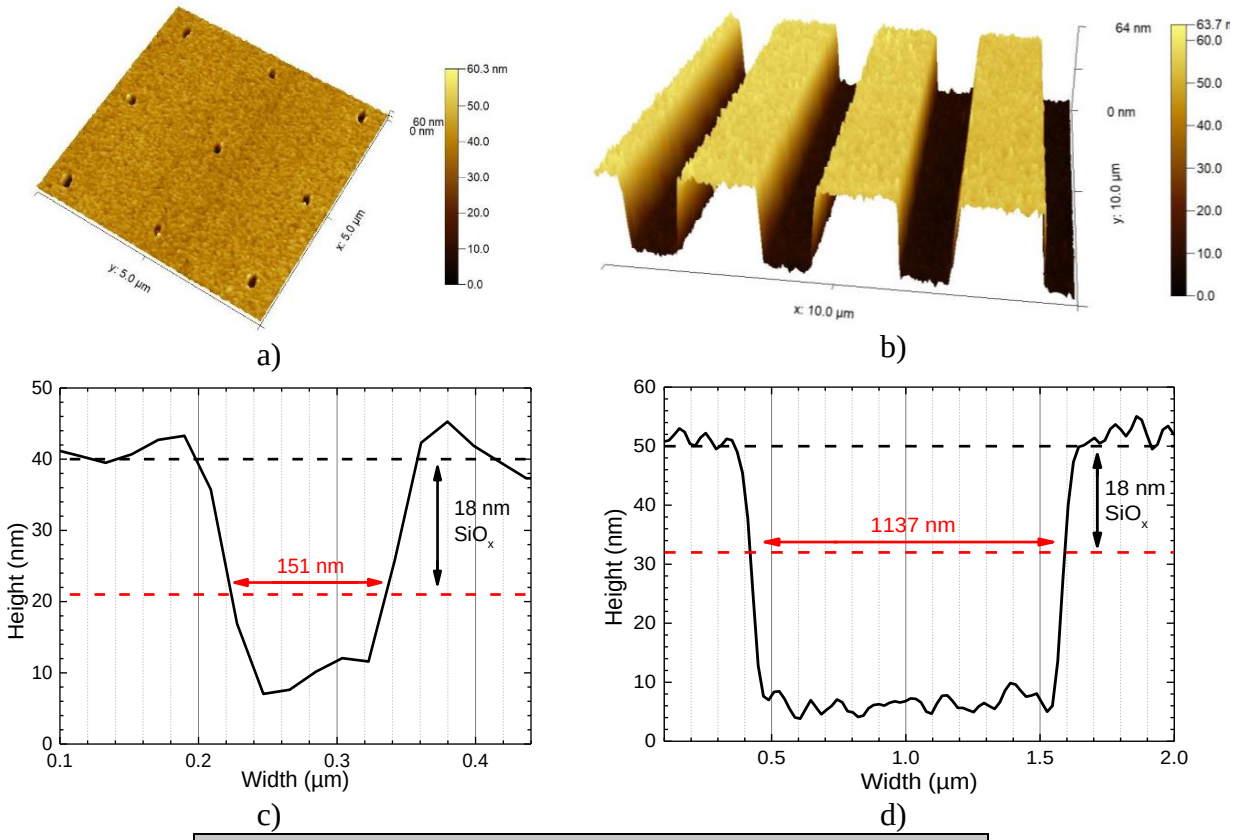

e)	Passivation area (%)	Contact width (nm)
PointContact	99.7	151 ± 22
LineContact	59.5	1137 ± 13

Figure 6 Representative AFM 3D image of: a) point contact; and b) line contact based substrates. Representative AFM cross-section plot of: c) point contact; d) line contact based substrates, where it is shown the SiO_x thickness (double black arrow) and the average contact width (double red arrow); and e) Contact width average and standard deviation values of both studied substrate architectures. Average values were taken in 9 patterns of the same AFM image. The passivation area for each device is also presented. Representative AFM images of the substrates were chosen based on the contact width value closer to the average contact width value.

List of Tables

Table 1 - Names of the substrates/devices used according to the passivation architecture.

	CIGS growth temperature (°C)	SiO_x Nanocontact Lithography
Ref	550/500	-
PointContact	550/500	E-beam
LineContact	550/500	Photolithography

Table 2 Crucial parameter values used in Silvaco ATLAS 2D electrical simulations. It is noted that for the passivated devices, it is represented the SRV value inside the nanocontacts (Mo/CIGS) and outside the nanocontacts (SiO_x/CIGS).

	R_c ($\Omega.cm^2$)	Defect density (cm^{-3})	R_b (%)	Doping density (cm^{-3})	SRV (cm/s)
Ref	1	2×10^{14}	20	3×10^{16}	Mo/CIGS 1×10^{7}
PointContact	0.1	1×10^{14}	45	5×10^{16}	Mo/CIGS 1×10^{7} SiO_x/CIGS 1×10^{2}
LineContact	0.1	1×10^{14}	45	5×10^{16}	Mo/CIGS 1×10^{7} SiO_x/CIGS 1×10^{2}